Nanostructural Evolution: From One-Dimensional Tungsten Oxide Nanowires to Three-Dimensional Ferberite Flowers

Weibing Hu,[†,‡,§] Yimin Zhao,[‡] Zuli Liu,[§] Charles W. Dunnill,[||] Duncan H. Gregory,[||] and Yanqiu Zhu*[,‡]

Department of Chemistry, Hubei Institute for Nationalities, Hubei, China, 445000, School of Materials, Mechanical and Manufacturing Engineering, The University of Nottingham, University Park, Nottingham NG7 2RD, U.K., Department of Physics, Huazhong University of Science and Technology, Wuhan, China, and WestCHEM, Department of Chemistry, Joseph Black Building, University of Glasgow, Glasgow G12 8QQ, U.K.

Received May 22, 2008. Revised Manuscript Received June 24, 2008

Based on a $W_{18}O_{49}$ nanowire template, iron-substituted $W_{18}O_{49}$ nanowires and $FeWO_4$ ferberite flowers have been generated by using mixed $FeCl_3$ and WCl_6 at different ratios in a simple solvo-thermal process employing cyclohexanol as the solvent. Detailed characterization by electron microscopy and spectroscopy has shown that increasing the $FeCl_3$ concentration during solvo-thermal synthesis promotes a morphological evolution from the long one-dimensional nanowires of the precursor through short Fe-containing $W_{18}O_{49}$ nanowires and two-dimensional platelets to three-dimensional flowers with sixfold symmetry. The driving force for these transformations is attributed to Fe inclusion in the $W_{18}O_{49}$ template at low Fe concentrations, which introduces internal stresses to the $W_{18}O_{49}$ nanowires. At high Fe concentrations, close to the stoichiometric composition of $FeWO_4$, the formation of the flower is triggered by the intrinsic sixfold symmetry of crystalline ferberite, via a combination of initial nanoblade nucleation and the competing self-assembly of neighboring parallel nanoblades. A similar solvo-thermal process has also been successful in the synthesis of $MnNb_2O_6$ bronze flowers, which exhibit structures with a morphology resembling a purposely carved microgear. Photoluminescent and magnetic properties of the products are also investigated.

1. Introduction

When sizes are reduced down to nanometer scale and shapes become more complex, materials tend to exhibit significantly enhanced functionalities in their properties than their commonly available bulk forms.[1] Highly renowned examples include core/shell semiconducting junctioned nanowires, which act as tuneable photonic light-emitting nanodiodes,[2] and branched quantum dots could enrich the understanding of entangled quantum states and quantum information processing in an individual nanostructure.[3] Consequently, structural complexity in nanomaterials has commanded the attention of many research groups worldwide and efforts have focused on mastering the synthetic routes to afford a host of novel and diverse nanomaterials, aiming to realize shape-, size-, and geometry-control.[4] After a decade of endeavors, numerous interesting nanostructures have been synthesized successfully via various approaches, and these low-dimensional structures include nanoparticles, nanorods/nanowires, nanotubes, nanobelts/nanosheets,[5] nanoferns/nanosaws,[6] and nanoflowers/microtrees.[7] It has been shown that growth of well-aligned 1-D nanowires/nanorods of ZnO and WO_3 could pave the way directly to nanodevice fabrication.[8] Solvo-thermal synthesis has been proven to be a facile and low-cost technique for production of nanostructures, including novel one-dimensional (1-D) nanocrystals.[5] In addition, solution-based soft-chemistry methods are capable of realizing new nanomaterials with different morphologies and stoichiometries controllably and reproducibly.[9] Further, solvo-thermal synthesis can yield nanomaterials with nonstoichiometric compositions,[10] which allows for compositional tailoring and tuning of the properties of resulting

* Corresponding author. E-mail: yanqiu.zhu@nottingham.ac.uk.
† Hubei Institute for Nationalities.
‡ The University of Nottingham.
§ Huazhong University of Science and Technology.
|| University of Glasgow.

(1) (a) Yang, P. D.; Wu, Y. Y.; Fan, R. *Int. J. Nanosci.* **2002**, *1*, 1–2. (b) Patzke, G. R.; Krumeich, F.; Nesper, R. *Angew. Chem., Int. Ed.* **2002**, *41*, 2446–2461.
(2) Hayden, O.; Greytak, A. B.; Bell, D. C. *Adv. Mater.* **2005**, *17*, 701–704.
(3) Milliron, D. J.; Hughes, S. M.; Cui, Y.; Manna, L.; Li, J.; Wang, L. W.; Alivisatos, A. P. *Nature* **2004**, *430*, 190–195.
(4) (a) Hyeon, T.; Lee, S. S.; Park, J.; Chung, Y.; Na, H. B. *J. Am. Chem. Soc.* **2001**, *123*, 12798–12801. (b) Liao, H. W.; Wang, Y. F.; Liu, X. M.; Li, Y. D.; Qian, Y. T. *Chem. Mater.* **2000**, *12*, 2819–2821. (c) Sun, S. H.; Zeng, H. *J. Am. Chem. Soc.* **2002**, *124*, 8204–8205.
(5) Choi, H. G.; Jung, Y. H.; Kim, D. K. *J. Am. Ceram. Soc.* **2005**, *88*, 1684–1686.
(6) (a) Zhu, Y. Q.; Hsu, W. K.; Zhou, W. Z.; Terrones, M.; Kroto, H. W.; Walton, D. R. M. *Chem. Phys. Lett.* **2001**, *347*, 337–343. (b) Lao, J. Y.; Wen, J. G.; Ren, Z. F. *Nano Lett* **2002**, *2*, 1287–1291.
(7) Zhu, Y. Q.; Hu, W. B.; Hsu, W. K.; Terrones, M.; Grobert, N.; Terrones, H.; Hare, J. P.; Kroto, H. W.; Walton, D. R. M. *Chem. Phys. Lett.* **1999**, *309*, 327–334.
(8) Yoo, S. J.; Lim, J. W.; Sung, Y.-E.; Jung, Y. H.; Choi, H. G.; Kim, D. K. *Appl. Phys. Lett.* **2007**, *90*, 173126.
(9) Gu, Z.; Zhai, T.; Gao, B.; Sheng, X.; Wang, Y.; Fu, H.; Ma, Y.; Yao, J. *J. Phys. Chem. B* **2006**, *110*, 23829–23836.
(10) Seo, J.-W.; Jun, Y.-W.; Ko, S. J.; Cheon, J. *J. Phys. Chem. B* **2005**, *109*, 5389–5391.

10.1021/cm801369h CCC: $40.75
Published on Web 08/06/2008

Table 1. Summary of the Solvo-thermal Processing Parameters and the Products

series no.	1	2	3	4	5	6	7	8	9
molar ratios (WCl_6:$FeCl_3$)	WCl_6 only	20:1	15:1	8:1	5:1	3:1	2:1	3:2	1:1
pH of solution	0.512	0.564	0.553	0.521	0.509	0.501	0.712	0.733	0.791
reaction parameters	200 °C, 16 h	200 °C, 16 h	200 °C, 16 h	200 °C, 16 h	200 °C, 16 h	200 °C, 16 h	200 °C, 16 h	200 °C, 16 h	200 °C, 16 h
morphology of key products	$W_{18}O_{49}$NWs[a]	Fe-doped NWs	Fe-doped NWs	bundled NWs + NWs	NW bundles + NFs[b]	NW bundles + desert rose	pure NFs	thick NFs	thick NFs
product phase(s)	monoclinic (M-) $W_{18}O_{49}$	M-$W_{18}O_{49}$	M-$W_{18}O_{49}$	M-$W_{18}O_{49}$, M-ferberite	M-$W_{18}O_{49}$, M-ferberite	M-$W_{18}O_{49}$, M-ferberite	M-ferberite	M-ferberite	M-ferberite

[a] NWs = nanowires. [b] NFs = flowers consisting of sixfolded nanoblades.

materials.[11] For example, metal-doped tungsten oxide nanowires may exhibit modified optical and electrical properties and it has been reported that Na-doped tungsten oxide nanowires become metallic.[12]

As one of the most important oxide nanomaterials, tungsten oxides and other transition metal oxides have been studied widely.[13] The wide indirect band gap of 2.6 eV makes WO_3 an ideal candidate for electronics and nanodevice applications.[14] Moreover, dilute magnetic semiconducting materials can be created by doping magnetic metals into bulk semiconducting tungstate. Only recently has the synthesis of low-dimensional (quasi zero-dimensional or 1-D) metal tungstates been reported (including $MnWO_4$, Bi_2WO_6, $CdWO_4$, and $FeWO_4$).[11,14] $FeWO_4$ (ferberite), an end member of the wolframite family ($FeWO_4$−$MnWO_4$ solid solution), is isostructural with wolframite (space group *P*2/*c*) and is known to semiconduct.[15] The wolframite structure consists of hexagonally close-packed oxygen with metal cations occupying some of the octahedral sites in an ordered way. These materials have previously been synthesized in bulk form via hydrothermal methods at temperatures ranging from 200 to 550 °C[16] and the structural and spectroscopic features of these phases have been well-documented.[17] Ferberites have also been analyzed for their possible application as anodes in photoelectrolysis and are promising materials for applications such as catalysis, photoluminescence, microwave windows, and humidity sensors.[18]

In this paper, we describe how, by using a solution-based soft-chemistry technique, it is possible to realize pure tungsten nanowires reproducibly, and then we extend the process to Fe-substituted tungstate nanowires and to elegant three-dimensional (3-D) flower-like nanostructures of $FeWO_4$. Furthermore, we also demonstrate briefly that this versatile technique is also applicable to the production of other complex nanostructures exemplified by $MnNb_2O_6$. The resulting products are characterized in detail. The key process parameters that determine the shape and morphology of the nanostructures are discussed and a growth mechanism is proposed to explain the flower formation. Finally, the photoluminescence properties of the nanowires and the magnetic behavior of the flowers are discussed.

2. Experimental Details

A preprepared clear brown solution of 0.1 g of WCl_6 (0.252 mmol, Aldrich, chemical pure) and 2 mL of absolute ethanol was transferred into a Teflon-lined high-pressure reaction vessel of 100 mL capacity. $FeCl_3$ (0.03 mL, 0.126 mmol, Aldrich, 45% water solution) and 40 mL of cyclohexanol (Aldrich) were added to the reaction vessel, which was then sealed and heated at 180−240 °C in a fanned Muffle Furnace for 8−20 h. The actual molar ratios of the $FeCl_3$ and WCl_6 used in this study, as well as the key process parameters and the main products, are summarized in Table 1. In the case of the $MnNb_2O_6$ synthesis, $MnCl_5$ was added to 9.3×10^{-3} M $NbCl_5$ cyclohexanol solution and the same procedures above were followed during solvo-thermal synthesis. After natural cooling to room temperature, the products were removed from the vessel and washed thoroughly with ethanol and deionized water several times in an ultrasonic bath to remove residual reagents and other possible impurities.

The as-prepared sample was pipetted onto a Si wafer or a holey carbon-coated Cu grid for further investigation using scanning electron microscopy (SEM Philips XL30) or transmission electron microscopy (TEM, JEOL 2000FX operated at 200 kV) respectively. Air-dried powder samples were then characterized by powder X-ray diffraction (XRD) (Siemens D500 X-ray diffractometer). A thin film of each powdered sample was deposited on a small Si wafer (10 mm × 10 mm) for spectroscopic measurements. Photoluminescence (PL) spectra were collected for the tungsten oxide nanowires using a Cary Eclipse fluorescence spectrophotometer with a Xe lamp as the excitation light source (excitation at 255 or 270 nm) at room temperature. Infrared (IR) spectra were recorded on a Perkin-Elmer 2000-FTIR spectrometer using a KBr supported sample wafer in a Pyrex vacuum IR cell. Raman spectra were recorded using a Renishaw Raman microscope, with an Ar laser excitation at a wavelength of 514.5 nm. The surface nitrogen content was characterized by X-ray photoelectron spectroscopy (XPS), using a Kratos AXIS ULTRA spectrometer with a monochromated Al kR X-ray source (1486.6 eV) operating at an emission current of 10 mA with an anode potential of 15 kV. The analysis chamber pressure used was better than 10^{-9} Torr. The magnetic susceptibility of the samples was investigated using a Quantum Design MPMS-XL 5T SQUID magnetometer. Accurately weighed flower samples were loaded into gelatine capsules and measurements were taken from 2 to 200 K using fields of 10 and 100 Oe under zero field

(11) Yu, S. H.; Liu, B.; Mo, M. S.; Huang, J. H.; Liu, X. M.; Qian, Y. T. *Adv. Funct. Mater* **2003**, *13*, 639–647.
(12) Shengelaya, A.; Reich, A. S.; Tsabba, Y.; Muller, K. A. *Eur. Phys. J. B* **1999**, *12*, 13–15.
(13) (a) Talledo, A.; Granqvist, C. G. *J. Appl. Phys.* **1995**, *77*, 4655–4666. (b) Meixner, H.; Gerblinger, J.; Lampe, U.; Fleischer, M. *Sens. Actuators, B* **1995**, *23*, 119–125. (c) Solis, J. L.; Saukko, S.; Kish, L.; Granqvist, C. G.; Lantto, V. *Thin Solid Films* **2001**, *391*, 255–260.
(14) Kloprogge, J. T.; Weier, M. L.; Duong, L. V.; Frost, R. L. *Mater. Chem. Phys.* **2004**, *88*, 438–443.
(15) Dresdner, H. C.; Escobar, C. *Z. Kristallogr., Bd* **1968**, *127*, S61–67.
(16) (a) Klevtsov, P. V.; Novgorodtseva, N. A.; Kharchenko, L. Yu. *Sov. Phys.-Crystallogr.* **1970**, *15*, 532–533. (b) Buhl, J. C.; Willgallis, A. *Chem. Geol.* **1986**, *56*, 271–279.
(17) (a) Griffith, W. P. *J. Chem. Soc. A* **1970**, 286–291. (b) Frost, R. L.; Duong, L.; Weier, M. *Spectrochim. Acta, A* **2004**, *60*, 1853–1859.
(18) (a) Qi, T.; Takagi, K.; Fukazawa, J. *Appl. Phys. Lett.* **1980**, *36*, 278–279. (b) Van Uibert, L. G.; Preziosi, S. *J. Appl. Phys.* **1962**, *33*, 2908–2908(c) Qu, W.; Wlodarski, W.; Meyer, J. U. *Sens. Actuators, B* **2000**, *64*, 182–188.

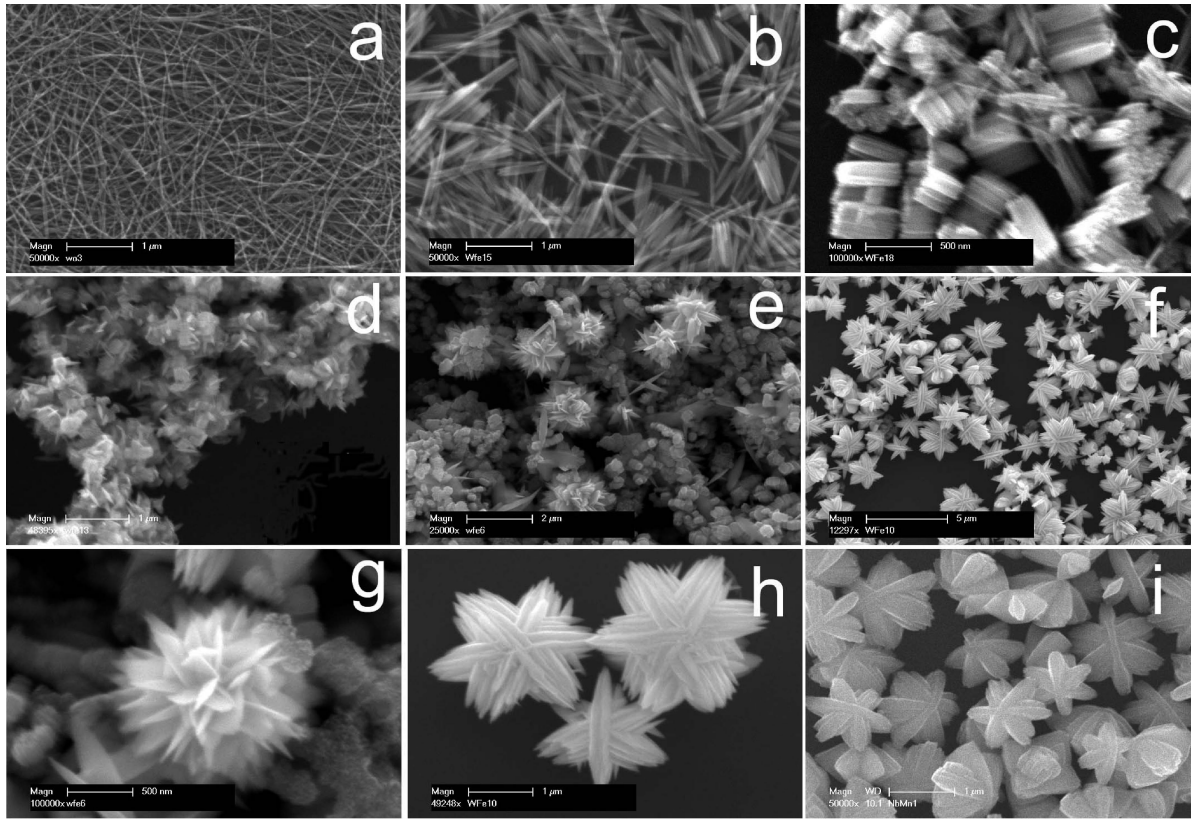

Figure 1. SEM images showing the geometry evolution from 1-D nanowires to 3-D flowers for different W:Fe (or Nb:Mn) concentrations.: (a) Pure $W_{18}O_{49}$ nanowires (**1**); (b) Fe-containing bundles of short nanowires (**2**); (c) short nanorod blocks (**3**); (d) randomly oriented nanoplatelets (**5**); (e) particles and localized blade formations (**6**); (f) $FeWO_4$ flowers (**7**); (g) desert rose structure of individual particle (**6**); (h) well-developed $FeWO_4$ flowers (**9**); and (i) pure $MnNb_2O_6$ flowers from a 1:1 ratio of Nb:Mn (**10**).

cooling (ZFC) conditions from room temperature and then under field cooling (FC) conditions over the same range.

3. Results and Discussion

3.1. Structural Characterization. Using WCl_6 as a starting material and cyclohexanol (bp 176 °C) as the solvent in a 200 °C hydrothermal process, we have easily achieved high-quality ultrafine (1−4 nm in diameter) $W_{18}O_{49}$ nanowires.[19] The high boiling point of cyclohexanol offers both the advantage of safer processing and thinner diameters for the product nanowires compared to that of an ethanol solvent as has been reported recently.[5,10,20] By introducing Fe ions into the system, we aim to take advantage of the 1-D WO_3 template to design new and compositionally modified 1-D nanomaterials with functionalized properties. In the course of study, it is shown that varying the Fe:W ratio has a profound impact on the geometry and morphology of the products (samples **1**−**9** in Table 1). Figure 1 shows the resulting nanostructures obtained under increasing Fe ion concentration, which demonstrates clearly the geometry evolution of the structures, from long and fine (bundled and ultra thin) $W_{18}O_{49}$ nanowires (Figure 1a) to short and densely bundled nanowire clusters (Figures 1b and 1c), to mixtures of short irregular nanowires and platelets (Figure 1d), through "desert rose" type structures (accompanied by many nanoparticles) (Figure 1e), and to, ultimately, completely converted 3-D flowers consisting of nanoblades(Figure 1f). At very low Fe/W molar ratios Fe inclusion has seemingly little effect on structure and the Fe-substituted $W_{18}O_{49}$ nanowires grow with aspect ratios similar to the pure tungsten oxide nanowires. With increasing iron concentration, the nanowires bundles become shorter and the aspect ratios decrease significantly until the rods form predominantly two-dimensional nanoplatelets (Figure 2c). The desert rose type structure consists of numerous irregular nanoplates stacking together randomly, exhibiting various shapes. An approximately spherical desert rose of ca. 1 μm in diameter is shown in Figure 1g. Increasing the Fe:W ratio further results in regular crystalline flowers with approximate sixfold symmetry, comprising multiple thin blades assembled in specific directions (Figure 1h). We have also monitored the pH values of the precursor solvents, and they appear to have no significant effect on the geometry evolution. Given that other physical parameters were invariant, the key factor dictating the morphology changes is thus believed to be the Fe concentration. Figure 1i exhibits another type of fully developed flower structure formed by $MnNb_2O_6$ (sample **10**). These basically resemble the ferberite flowers, but the blade or layer numbers in each of the six directions seem to be significantly reduced. Each blade appears to be fairly thick, resembling a purposely carved micromechanical gear. This result demonstrates that other combinations of transition metals can be used in the solvo-thermal generation of

(19) Zhao, Y. M.; Hu, W. B.; Xia, Y. D.; Smith, E. F.; Zhu, Y. Q.; Dunnill, C. W.; Gregory, G. H. *J. Mater. Chem.* **2007**, *17*, 4436–4440.
(20) Polleux, J.; Antonietti, M.; Niederberger, M. *J. Mater. Chem.* **2006**, *16*, 3969–3975.

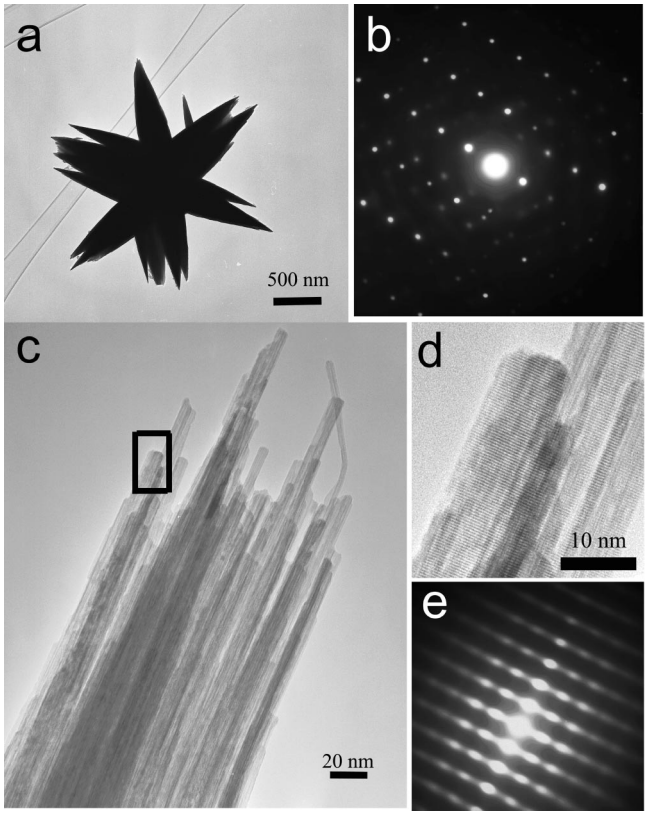

Figure 2. TEM images of (a) a single $FeWO_4$ flower and its electron diffraction pattern (b); (c) the pronounced bundled feature of the Fe-containing $W_{18}O_{49}$ nanowires; (d) the selected area in (c) at high resolution, exhibiting well-crystallized lattice fringes; and (e) electron diffraction pattern of the bundles, showing the aligned characteristics of the nanowires.

complex compounds with novel nanostructures. We will focus on the ferberite nanostructures in this context.

According to EDX analysis during TEM examination, the chemical composition of the flowers varies slightly from sample to sample, corresponding to Fe_xWO_4 in which x ($0 < x \leq 1$) depends upon the initial Fe:W molar ratio. In any one batch of samples, the flowers are generally chemically homogeneous and morphologically and dimensionally alike, whereas within a specific flower its composition also appears to be fairly uniform for different blades aligned in different directions. Figure 2a shows a typical TEM image of a flower, which, at high magnification, appears to be asymmetric, compared with the SEM images shown in Figure 1. In fact, tilting the sample holder normally leads to a perfectly symmetric flower (Supporting Information, Figure S1). Moreover, during the tilting and rotating process we have also revealed that these nanoblades generally project a symmetric oval shape. Furthermore, selected area electron diffraction (SAED) confirms, perhaps surprisingly, that the flowers consist of monophasic single crystals, in spite of the high complexity of the multibladed configuration, Figure 2b. At low Fe:W molar ratio (1:20), the bundled nanowires (**2**) are fairly uniform in diameter (Figure 2c), being well-crystallized single crystals, as shown in the high-resolution image in Figure 2d. The SAED pattern (Figure 2e), dots being fused together becoming lines with identical distance, suggests that in this particular bundle these aligned nanowires have predominantly adopted the same orientation, which presumably originates at the growth stage rather than subsequent to solvo-thermal processing. The well-defined lattice fringe within the bundles with a spacing of 0.38 nm is in line with the $W_{18}O_{49}$ (002) spacing. In this context, the evidence for monophasic single crystals shown in Figure 2, together with the elemental analysis for the bundled nanowires (Supporting Information, Figure S2) seems to suggest $W_{18}O_{49}$ nanowire templated formation for the low-concentration Fe-substituted tungstate nanostructures. It is noteworthy that these slightly thicker and shorter Fe-modified nanowires appear to be straighter and more rigid than the pure $W_{18}O_{49}$ nanowires (Figure 1a), which implies the inclusion of Fe in the lattice may have caused structural stresses within the $W_{18}O_{49}$ lattice.

When the W:Fe ratio reaches 2:1, the resulting materials (**7**) consist of almost 100% pure flowers. XRD examination further reveals that these flowers are typically monoclinic $FeWO_4$ (ICDD card 01-085-1354), namely, ferberite, as shown in Figure 3. At different W/Fe molar ratios, e.g., 15:1 (**3**) as shown in Figure 3b, the Fe-containing nanowires seem to have gradually altered the original tungsten oxide crystallinity, as compared to the pure $W_{18}O_{49}$ nanowires (Figure 3a). For ultrathin $W_{18}O_{49}$ nanowires bundles synthesized via solvo-thermal synthesis, it is not easy to match the experimental, low-intensity XRD patterns to patterns from bulk $W_{18}O_{49}$, largely because of the size and shape of the wires (small diameters and large aspect ratios leading to peak broadening and preferred orientation). It proved even more difficult to match the Fe-containing tungsten oxide nanowires. For example, the XRD profile of sample (**3**) from the 15:1 W/Fe ratio precursors shows significant peak broadening and diminished intensity for the $W_{18}O_{49}$ reflections; notably, the (010) is no longer the strongest reflection, which is associated with the shortened morphology of the nanowires. Meanwhile, a peak at about $2\theta = 33°$ becomes stronger, which could be assigned to the emerging (111) reflection from ferberite. Nevertheless, Figure 3b seems to suggest that an intermediate growth stage may occur as a result of Fe inclusion. In fact, the crystallinity of the $W_{18}O_{49}$ nanowire samples diminished completely as the W:Fe ratio decreases to 10:1. It is thus clear that the Fe addition mediates the morphological evolution and gradually leads to the dominant feature of ferberite in the final products, which is evidenced by the well-matched XRD pattern shown in Figure 3c.

3.2. Raman, IR, and XPS Characterization. The Raman spectra for ferberite has previously been reported on only two occasions,[18a] with a focus on the impure mineral forms which normally contain Mn or Mg. The present results (Figure 4) based on the single-phase $FeWO_4$ flowers more closely resemble a recently reported spectrum of laboratory-synthesized ferberite.[18b]There are three Raman shifts at 215, 281, and 704 cm^{-1}, which are identical to the literature. The first two low wavenumber bands have been assigned to the $\nu_4(B_g)$ mode, and the 704 cm^{-1} band to $\nu_3(B_g)$ and $\nu_3(E_g)$. A band is also observed at 386 cm^{-1}, which is close to the previously recorded bands at 379 and 388 cm^{-1}, both being assigned to the $\nu_4(B_g)$ mode. The weak band at 591 cm^{-1} has not previously been assigned. The two sharp bands at 129 and 802 cm^{-1} have not been observed previously for

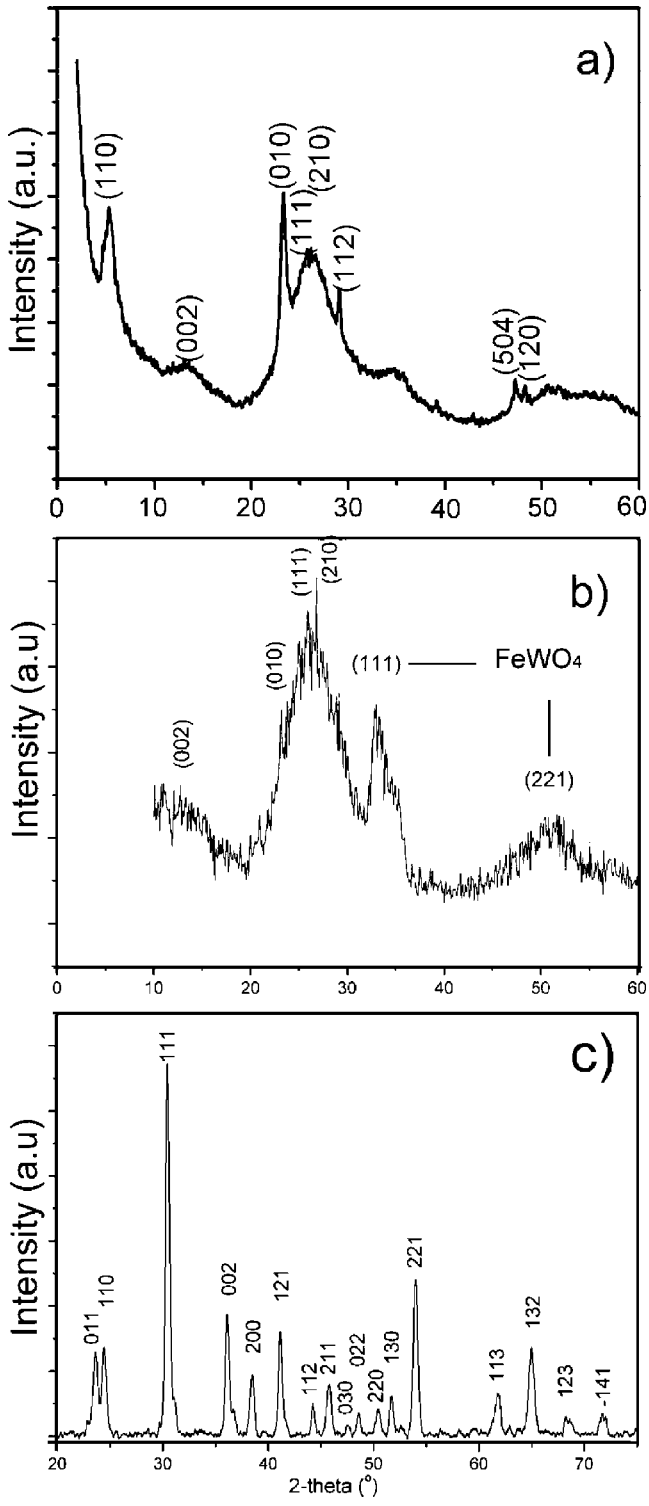

Figure 3. XRD profiles of (a) $W_{18}O_{49}$ nanowires (**1**) and (b) Fe-doped $W_{18}O_{49}$ (**3**) and $FeWO_4$ flowers (**7**). The two marked reflections in (b) correspond to those from ferberite.

ferberite, and interestingly they are also present in the low Fe ratio nanowires. These two bands may be associated with the antisymmetric and symmetric A_g modes of the WO_2 groups, respectively. By comparison, Frost et al. have previously observed a similar band at 126 cm^{-1} for hübnerite ($MnWO_4$) crystals,[18] while a similar band at 134 cm^{-1} also occurred for monoclinic WO_3 crystals, which was ascribed to the ν(W−O−W) mode;[22] thus it remains unclear if this band arose from tungsten oxide or ferberite. The 802 cm^{-1}

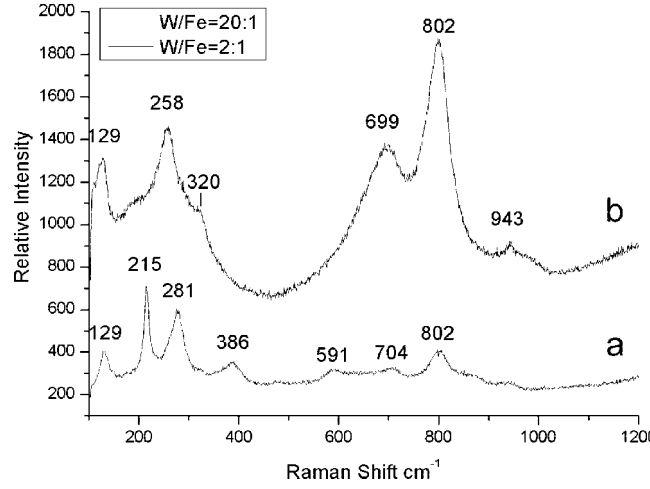

Figure 4. Raman spectra of (a) Fe-containing $W_{18}O_{49}$ (**2**) (W/Fe = 20:1) and (b) $FeWO_4$ ferberite (**7**) (W:Fe = 2:1).

band may correspond to the 811 cm^{-1} band observed for laboratory-synthesized bulk ferberite, which was assigned to the $\nu_1(A_g)$ mode. However, because the low Fe concentration nanowires (**2**) (W:Fe = 20:1) are structurally closer to $W_{18}O_{49}$ than to $FeWO_4$, it is more appropriate to compare them with monoclinic $W_{18}O_{49}$. Indeed, we found that the Raman bands at 129, 215, 320, and 802 cm^{-1} (Figure 4a) are fairly close to that reported for *m*-WO_3 particles and thin films with bands at 134, 218, 327, and 807 cm^{-1},[21,22] and they are all shifted to slightly lower frequencies in the nanowire sample. This result seems to suggest that the low Fe-content nanowires have basically retained their original lattice structures, exhibiting a $W_{18}O_{49}$ templating characteristic.

FT-IR spectra of the resulting materials exhibit several peaks at 919, 854, 815, and 629 cm^{-1} for the flowers and 976, 914, 816, 782, 706, and 649 $cm^{-1}$for the low W:Fe ratio nanowires, Figure 5. For the ferberite flowers, the broad bands at 815 and 629 cm^{-1} are similar to those reported for synthetic ferberite, whose bands occur at 818 and 625 cm^{-1}, being assigned to Ag or Au and deformation mode, respectively.[18] The Fe-doped $W_{18}O_{49}$ nanowires exhibit several bands that may also be assigned to the ferberite, such as the shoulder at 816 and the broad band at 706 cm^{-1}. Similar to the Raman spectra, the FT-IR features of these nanowires are compared with the $W_{18}O_{49}$, and bands at 816 and 649 cm^{-1} correspond to the O−W−O vibration mode and the W−O stretching band, respectively.[23]

The surface characteristics of nanostructures with different Fe ratios have been assessed by XPS, and the results are shown in Figure 6 for selected materials. For low Fe ratio nanowire bundles (**3**) (W:Fe = 15:1), it is surprising to discover that very little Fe is detected on the nanowire surface, only W and O, while for the high Fe content flower sample (**7**) (W:Fe = 2:1), Fe was detected. This result seems to further suggest that the Fe inclusions indeed occur within the nanowire lattice, as indicated by the EDX analysis to

(21) Daniel, M. F.; Desbat, B.; Lassegues, J. C.; Gerand, B.; Figlarz, M. *J. Solid State Chem.* **1987**, *67*, 235–247.
(22) Fang, G.; Liu, Z.; Yao, K. L. *J. Phys. D* **2001**, *34*, 2260–2266.
(23) Badilescu, S.; Ashrit, P. V. *Solid State Ionics* **2003**, *158*, 187–197.

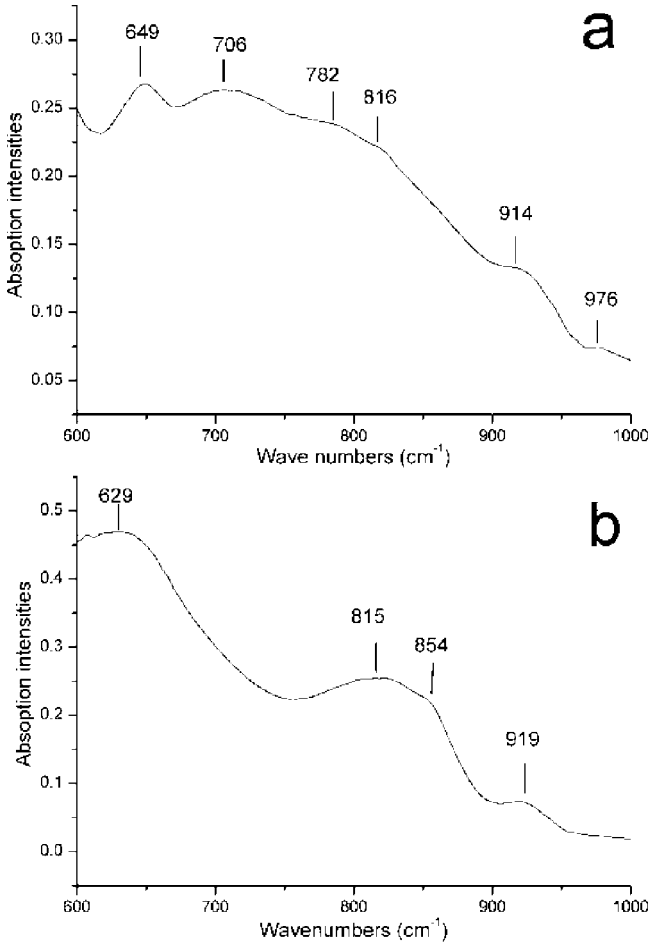

Figure 5. FT-IR absorption spectra of (a) Fe-containing $W_{18}O_{49}$ nanowires (**2**) and (b) $FeWO_4$ flowers (**9**).

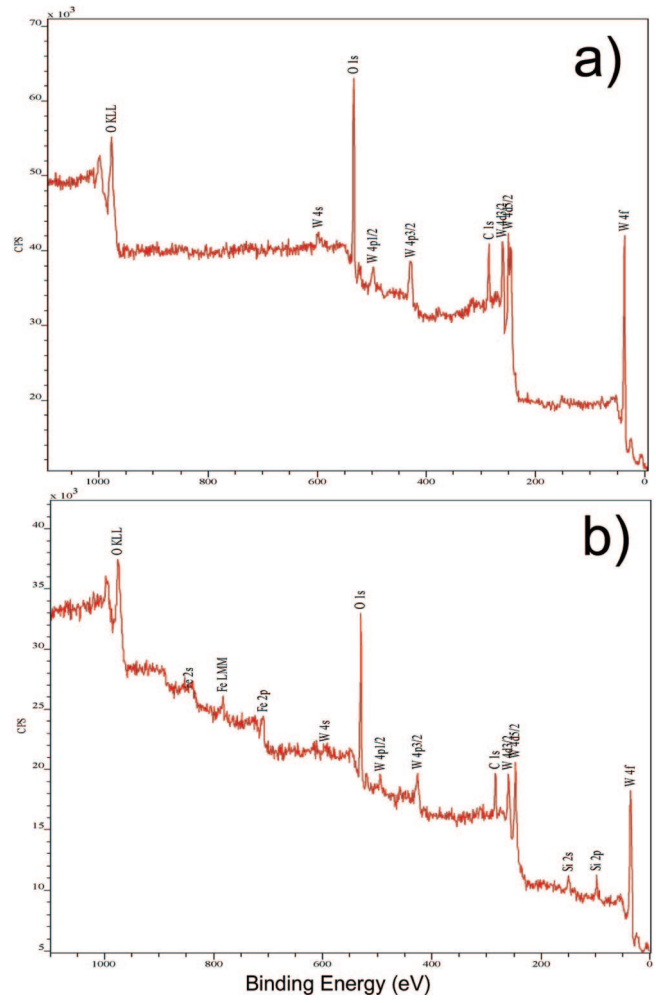

Figure 6. XPS survey spectra for (a) the Fe-containing $W_{18}O_{49}$ nanowires (**3**) (W:Fe = 21:1) and (b) the $FeWO_4$ flowers (**7**) (W:Fe = 2:1).

individual nanowires, rather than staying on the surface, which could lead to the explanation as to why the nanowires became much more rigid, shorter, and straighter, as evidenced by the reduced (010) intensity in Figure 2b. Inevitably, as the concentration of Fe (presumably as Fe^{3+} or Fe^{2+} as the Fe 2p signal occurred at 710.7 eV in the XPS is noisy and inclusive about its state) reaches a certain level, the $W_{18}O_{49}$ structure (likely defective and under significant crystalline strain) cannot be sustained and the new $FeWO_4$ phase is formed.

3.3. Growth Mechanism. The growth of the nanostructures described above is a complicated process. It is obvious that two key stages and a series of intermediate phases might be involved. The two key stages can be defined as the growth of the 1-D nanowires (Figure 1a) and the formation of the flowers (Figures 1f and 1i); while the intermediate stages, as revealed by the SEM images in Figure 1, can be briefly classified as the formation of shortened bundles (Figure 2b), the development of large bundled blocks (Figure 1c), and the random platelet formation which eventually leads to the 6-fold symmetry flowers. The investigation of the solvothermal parameters described in Table 1 provides valuable information for the understanding of the morphology evolution. The solvo-thermal synthesis and 1-D growth of pure $W_{18}O_{49}$ nanowires bundles from tungsten salts have been reported recently.[5,10,19,24] The growth direction of the monoclinic $W_{18}O_{49}$ nanowires is ⟨010⟩ according to the ED results. Although there is no direct evidence to show the exact role of the chemical species of the cyclohexanol on the nuclei surface, it is apparent that they must have played an important part in hindering the development in the ⟨002⟩ direction to achieve the 1-D growth. A simple comparison shows that hydrothermal conditions (i.e., using water as solvent) yield only 3-D tungsten oxide particles without any dominant growth direction.[9] Many surfactants or alkaline salts additives played a comparable role during the solvo-thermal synthesis of 1-D tungsten oxide nanowires.[9]

The progressive development of the short and large bundled blocks and the random platelets (Figures 1c and 1d) as the $FeCl_3$ concentration is increased is reminiscent of work by Gu and co-workers for simultaneous ribbon growth when K_2SO_4 is used as an additive.[9] In this previous work, the authors discussed an oriented-attachment mechanism proposed by Penn and Banfield to explain the growth of various oriented and hierarchical nanostructures via self-assembly of nanocrystals.[25] Gu et al. attribute ribbon formation to the random aggregation and recrystallization of individual

(24) Polleux, J.; Gurlo, A.; Barsan, N.; Weimar, U.; Antonietti, M.; Niederberger, M. *Angew. Chem., Int. Ed.* **2006**, *45*, 261–265.
(25) (a) Penn, R. L.; Banfield, J. F. *Science* **1998**, *281*, 969–971. (b) Penn, R. L.; Oskam, G.; Strathmann, T. J.; Searson, P. C.; Stone, A. T.; David, R. V. *J. Phys. Chem. B* **2001**, *105*, 2177–2182.

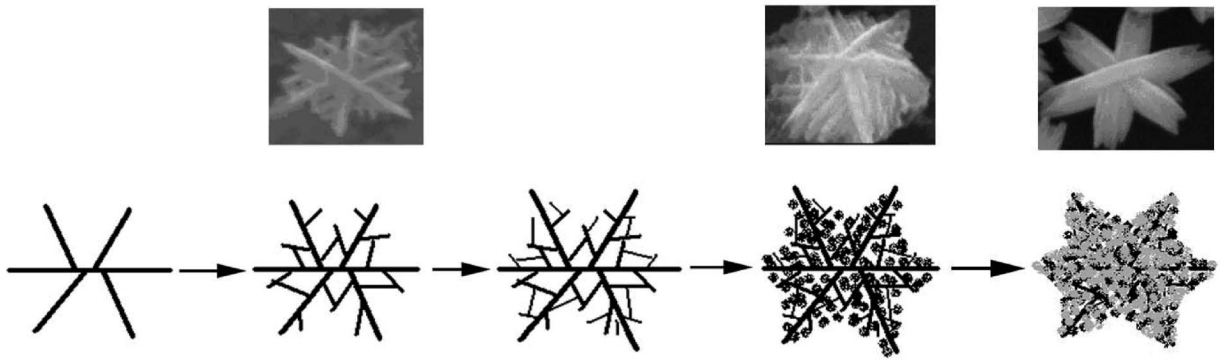

Figure 7. A schematic drawing illustrating different stages of the $FeWO_4$ flower formation via sustained development of skeletons (plates) and aggregation (nanowires and particles). SEM images were taken from samples after different reaction times.

aligned nanowires to form large single-crystalline ribbons. During aggregation, perfectly aligned crystalline planes or dislocations at the contact areas between adjacent nanowires play an essential role in the final morphology of the ribbons. It is possible that increasing the Fe concentration within the tungstate nanowires described herein could cause severe crystalline defects, by analogy to those created by the presence of K or Rb in the earlier work.[9] This process may then lead to the formation of the random nanoplates in the Fe−W−O system.

By further increasing of the Fe concentration in the system, the template influence of the $W_{18}O_{49}$ nanowires gradually disappears, superseded by the sixfold symmetry dominant in the crystallography of $FeWO_4$. From random platelets, such as the desert rose formations, to flowers, the only variable synthesis parameter was the Fe concentration; however the entire system can be viewed as consisting of two different phases: $W_{18}O_{49}$-based platelets and $FeWO_4$-based platelets. By increasing the amount of Fe^{2+} in the liquid sufficiently, e.g., W:Fe = 2:1, it is possible to form pure stoichiometric $FeWO_4$ flowers (Figure 1f and as verified by XRD, Figure 3). During this stage, the crystal habits of the ferberite will play the leading role. Although we so far have no direct evidence that the flower formation is either via the aggregation of 1-D nanowires and particulate nanocrystals or via a sustained development about an original single nucleus, it seems that both routes may have coexisted during the synthesis. When a localized stoichiometric ratio is reached during solvo-thermal synthesis, the formation of the flowers is believed to originate from, and be controlled by, the six intrinsically equivalent growth directions, leading to flowers of high symmetry (Figure 1). This supports the sustained development mechanism. However, the existence of some asymmetric or branched plates, i.e., underdeveloped flowers (Figure 7), appears to support the aggregation mechanism for the final flowers. Nevertheless, the reduced plate numbers in one of the six directions in the final flower confirm that self-assembled aggregation indeed occurs (Figure 1h), at least at a later stage.

Based on these analyses, we propose that the growth of the flower structures is initiated by a simple nucleus which was meditated by its intrinsic crystal orientations to further develop into sixfold plates which act as a skeleton of the flower. Competing growth and self-assembly along one particular direction might lead to several closely connected plates parallel to each other, while the original skeleton plate remained as the leading plate; see Figure 2a. At a later stage (prolonged synthesis time), aggregation of plates or aggregation of plates and floating nanowire bundles probably occurs, resulting in fully developed flowers. However, the dominant growth for the flower seems to be controlled by the intrinsic crystal orientation, as in such a way the pronouncedly similar and regular flower morphology can be easily explained. A typical example is the fully grown gearlike $MnNb_2O_6$ flowers (Figure 1i) in which the plate component structures are no longer recognizable in the six teeth of the gear. A schematic illustration of the proposed $FeWO_4$ flower formation process is shown in Figure 7, at different stages, from skeleton to fully developed flower.

3.4. Physical Properties. Figure 8 shows the PL spectra of pure $W_{18}O_{49}$ (**1**) and one of the Fe-doped tungsten oxide (W:Fe = 15:1; **3**) nanowire samples excited by a Xe lamp with a wavelength of 255 nm. For the pure nanowire samples, there are two typical characteristic peaks: an ultraviolet (UV) emission peak at 369 nm (3.36 eV) that is due to the band−band transition of the wide band gap tungsten oxide and a blue emission peak at 422 nm (2.94 eV) which has been previously attributed to oxygen vacancies or defects in tungstate nanowires and nanorods.[26] Similarly, the Fe-containing sample also showed two major peaks (Figure 8b), but the strength of the UV emission peak is much weaker and appears at 349 nm (3.56 eV), with an even weaker broad peak at 346 nm (3.58 eV) for the $FeWO_4$ samples (**7**) (Figure 8c),. The blue emission peaks (423 nm) exhibit almost no change across samples. However, the UV emission appears at a shorter wavelength, which indicates an increased band gap in the doped nanowire samples compared to that of (**1**). Comparing with the general indirect band gap of 2.6 eV for pure bulk WO_3, and 2.0 eV for bulk $FeWO_4$,[27] we recognize that the 3.36 and 3.56 eV band gaps for the ultrathin $W_{18}O_{49}$ nanowires (**1**) and the Fe-containing samples (**3**) and (**7**) are significantly wider.

(26) (a) Feng, M.; Pan, A. L.; Zhang, H. R.; Li, Z. A.; Liu, F.; Liu, H. W.; Shi, D. X.; Zou, B. S.; Gao, H. J. *Appl. Phys. Lett.* **2005**, *86*, 141901−1−3. (b) Lee, K.; Seo, W. S.; Park, J. T. *J. Am. Chem. Soc.* **2003**, *125*, 3408–3409.

(27) Ejima, T.; Banse, T.; Takatsuka, H.; Kondo, Y.; Ishino, M.; Kimura, N.; Watanabe, M.; Matsubara, I. *J. Lumin.* **2006**, *119−120*, 59–63.

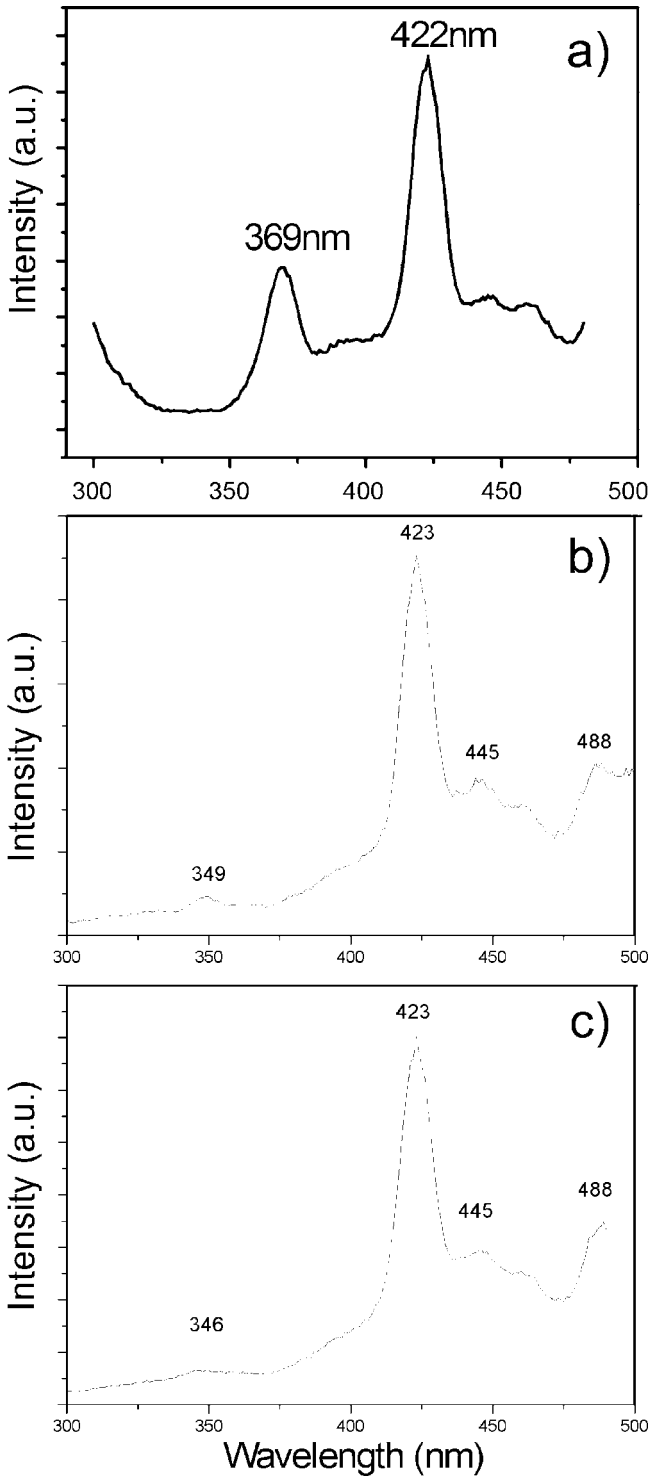

Figure 8. PL spectra of (a) pure $W_{18}O_{49}$ (**1**), (b) Fe-containing tungsten oxide nanowires (**3**) (W:Fe = 15:1), and (c) $FeWO_4$ flowers (**7**), excited by a Xe lamp at 255 nm wavelength.

The temperature-dependent magnetic behavior of the $FeWO_4$ flowers was assessed by SQUID magnetometry. The mass susceptibility χ_g vs temperature plot (Figure 9a) shows that the FC and ZFC curves almost perfectly overlap and that there is an increase in χ_g with decreasing temperature until the susceptibility reaches a broad maximum at 60 K and decreases subsequently with decreasing temperature. The broad maximum is typical of an antiferromagnetic transition and is consistent with bulk ferberite $FeWO_4$, with the

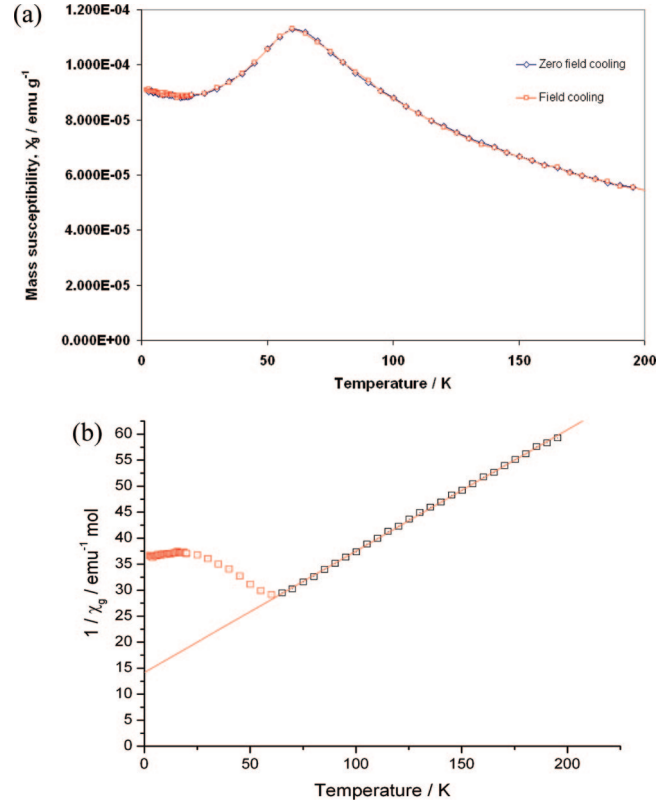

Figure 9. (a) χ_g vs temperature and (b) the linear fit to the inverse molar susceptibility vs temperature above T_N for $FeWO_4$ flowers (**7**).

exception that in the bulk the Néel temperature (T_N) is reported as either 66 K[15] or 75 K,[28] both higher than the value of T_N for (**7**). The molar susceptibility above T_N can be fit very well to the Curie−Weiss expression, $\chi = C/(T + \theta)$ (Figure 9b), yielding a value of $\theta = 60.8$ K and $C = 4.285$ emu mol^{-1} K corresponding to $\mu_{eff} = 5.88\ \mu_B$ for Fe. The value of the effective moment is higher than the expected spin-only moment for high-spin Fe^{2+} in an octahedral coordination (4.90 μ_B). Given that $FeWO_4$ contains W(VI) and there is no precedent mechanism for oxidation in (undoped) ferberite, the results suggest a significant orbital contribution to the moment for Fe(II) and values in excess of 5 μ_B have been observed for iron in bulk $FeWO_4$ in earlier studies.[29] The reduction in T_N compared to bulk ferberite is almost certainly size-mediated and not likely to be a simple relationship given the complex geometry of the flowers. Recent studies have correlated the changes in magnetic ordering temperatures to finite-size dependent factors[30] and, for example, reduced transition temperatures in iron-containing magnetic nanomaterials, such as the Morin transition in hematite nanoparticles and nanowires, have been previously observed.[31] Perhaps more pertinent still are the striking size effects evident for antiferromagnetic, monoclinic CuO nanoparticles, where T_N drops by 20% from bulk to 14 nm CuO

(28) Matres, E.-G.; Stusser, N.; Hofmann, M.; Reehuis, M. *Eur. Phys. J. B* **2003**, *32*, 35–42.
(29) Obermayer, H. A.; Dachs, H. *Solid State Commun.* **1973**, *12*, 779–784.
(30) Lang, X. Y.; Zheng, W. T.; Jiang, Q. *Phys. Rev. B* **2006**, *73*, 224444.
(31) Zhao, Y. M.; Dunnill, C. W.; Zhu, Y. Q.; Gregory, D. H.; Kockenberger, W.; Li, Y. H.; Hu, W. B.; Ahmad, I.; McCartney, D. G. *Chem. Mater.* **2007**, *19*, 916–921.

and by a further 70% when the diameter is reduced by a further 4 nm.[32] For the flowers, the size of the nanoplates is about 2 μm long while their width and thickness are rather small, about 100 nm and a few tens of nanometers, respectively. Therefore, the relatively small ($\approx$10%) decrease in T_N in the ferberite flowers over the bulk material here is consistent with their size and this earlier analysis of CuO. Further investigation of magnetism in terms of controlling size and geometry will be a very interesting subject.

4. Conclusions

Using mixed chlorides in a simple solvo-thermal process, we have successfully produced Fe-containing nanowires and elegant ferberite flowers at different $FeCl_3$ and WCl_6 ratios. The $FeCl_3$ concentration appears to play a determining role in the morphological evolution from nanowires to platelets and eventually to flowers with sixfold symmetry. The formation mechanism for the ferberite flowers is proposed as a combination of the initial nanoblade nucleus and the competing self-assembly of neighboring parallel nanoblades. The $FeWO_4$ flowers exhibit a broad antiferromagentic transition at $T_N = 60$ K that is depressed compared to that of bulk ferberite. The solvo-thermal process has also been extended to the synthesis of flowers of $MnNb_2O_6$, with gearlike morphology. These novel forms of nanomaterials may find applications in a wide range of nanodevice constructions.

Acknowledgment. W.B.H. thanks the University of Nottingham for hosting him to carry out the synthesis research work. Y.Q.Z. thanks the EPSRC for financial support. Special thanks to Dr. Y. Jin for the PL measurements. D.H.G. thanks the EPSRC for a DTA studentship for C.W.D.

Supporting Information Available: TEM images and EDX profiles (PDF). This material is available free of charge via the Internet at http://pubs.acs.org.

CM801369H

(32) Zheng, X. G.; Xu, C. N.; Nishikubo, K.; Nishiyama, K.; Higemoto, W.; Moon, W. J.; Tanaka, E.; Otabe, E. S. *Phys. Rev. B* **2005**, *72*, 014462.